

AJKFLUIDS2019-5473

WINGTIP VORTEX STABILITY AND CONTROL USING MEAN FLOW PERTURBATION

Andrew L. Bodling

Air Force Research Laboratory
Wright-Patterson AFB, OH 45433
Email: andrewbodling@gmail.com

Daniel J. Garmann *

Air Force Research Laboratory
Wright-Patterson AFB, OH 45433
Email: Daniel.Garmann@us.af.mil

ABSTRACT

Wingtip vortices generated by aircraft are the source of induced drag. Therefore, flow control devices such as winglets have been created to reduce the impact of tip vortices and consequently improve the wings performance. To use other flow control devices such as periodic heat-flux sources, the receptivity to the actuator must be fully optimized to be effective. The optimization process includes actuator placement, frequency selection and spatial modulation. The Mean Flow Perturbation (MFP) technique is a linear stability analysis that can be used to understand the receptivity of base flows to small perturbations. Its advantage over other linear stability analyses is that it can be applied fairly easily to complex 3-D flows in a relatively efficient manner, embedded within traditional flow-solver frameworks. This technique can help in gaining a better understanding of the receptivity of a flow control actuator that is used to control a complex 3-D flow. The current study seeks to apply the MFP technique to the author's previous work on unsteady tip vortices. The aspect-ratio-four, rounded-tip wing has a NACA0012 section and operates at a Reynolds number of $Re = 2 \times 10^5$ and incidence of $\alpha = 12^\circ$. The objective is to uncover the least stable mode shapes and frequencies of the structure using MFP in hopes of informing future flow control design techniques. At these conditions, the MFP shows a dominant least stable frequency and mode shape that occurs near the trailing edge of the wingtip. A region near the incipient separation of the vortex also showed with a definitive spatial wavelength that may be susceptible to tailored control.

INTRODUCTION

Wingtip vortices generated by aircraft are the source of induced drag. Since this adversely effects the aerodynamic performance of the wing, flow control of wingtip vortices are an extremely important research topic. There has been extensive work to try to control wingtip/edge vortices, with an excellent comparative review provided in Ref. [1]. Some of the common flow control methods used to control wingtip vortices are continuous blowing and suction, unsteady blowing, small-aspect-ratio jets, bleed, plasma actuators and control surfaces. Although there has been much progress made with these flow control methods, the flow control design process is very empirical in nature. The complex 3-D wingtip vortex structure leads to many interrelated parameters to consider in flow control design. For example, studies have been done to study the parameters of continuous blowing from high aspect ratio jets near the wingtip, including offset, canted slots (blowing at an angle to the wing's plane), longitudinal position, blowing coefficient, etc [2, 3]. Adding more to the complexity, an optimized flow control device may not work well at off-design flow conditions or with different tip shapes.

The empirical nature of wingtip flow control design underscores the need for a more informed methodology to quickly isolate regions of the flow that are most receptive to control and identify spatial modes and frequencies that are intrinsically unstable across that region. This type of flow information may be exploitable by tailored flow control techniques, and would greatly focus the otherwise large-parameter design space towards the most effective and rational control. The Mean Flow Perturbation (MFP) technique is a linear stability analysis that can

* Address all correspondence to this author.

be used to understand the receptivity of base flows to a small perturbation [4]. Ranjan *et al.* [4] showed that for MFP, in certain circumstances the results from a global stability analysis can be recovered. However, its advantage over other linear stability analyses is that it can be applied fairly easily to complex, fully three-dimensional flows in a relatively efficient manner. Applied to wingtip vortex control, this technique could uncover the spatial layout and forcing frequencies for an actuator operation to target the most susceptible modes of the tip vortex.

The current study seeks to apply the MFP technique to a wingtip vortex problem previously studied by the authors [5]. The objective is to better understand the least stable mode shapes and frequencies and apply flow control based off of the results from the MFP analysis.

NUMERICAL METHODOLOGY

Flow Solver

The MFP method is implemented into the compressible Navier-Stokes solver, FDL3DI [6]. The governing fluid flow equations (solved by FDL3DI), after performing a time-invariant curvilinear coordinate transform $(x, y, z) \rightarrow (\xi, \eta, \zeta)$, are written in a strong conservation form as

$$\frac{\partial}{\partial t} \left(\frac{\mathbf{U}}{J} \right) + \frac{\partial \hat{\mathbf{F}}_I}{\partial \xi} + \frac{\partial \hat{\mathbf{G}}_I}{\partial \eta} + \frac{\partial \hat{\mathbf{H}}_I}{\partial \zeta} = \frac{1}{Re} \left[\frac{\partial \hat{\mathbf{F}}_v}{\partial \xi} + \frac{\partial \hat{\mathbf{G}}_v}{\partial \eta} + \frac{\partial \hat{\mathbf{H}}_v}{\partial \zeta} \right], \quad (1)$$

where J is the Jacobian of the coordinate transformation, $\mathbf{U} = \{\rho, \rho u, \rho v, \rho w, \rho E\}$; the expressions for inviscid flux terms, $\hat{\mathbf{F}}_I, \hat{\mathbf{G}}_I, \hat{\mathbf{H}}_I$ and viscous flux terms, $\hat{\mathbf{F}}_v, \hat{\mathbf{G}}_v, \hat{\mathbf{H}}_v$ are provided in Ref. [6]. We perform ‘implicit’ LES (ILES) simulations using FDL3DI by employing sixth-order spatial accuracy, eighth-order low pass filters, and a second order, implicit time integration scheme.

Mean Flow Perturbation (MFP)

The MFP method, in conjunction with dynamic mode decomposition (DMD), is used to find relevant instability modes, their growth rates and associated frequencies [4]. The MFP method is implemented into FDL3DI, which essentially allows for a time integration of the linearized Navier-Stokes equations. For the MFP algorithm, an initial white noise perturbation is given to the time-averaged base flow, \mathbf{Q}_b , near the leading edge of the wing. A perturbation amplitude of five orders of magnitude smaller than the free-stream values is used to maintain a linear evolution of the perturbation. To ensure consistency between the base flow and perturbation solutions, the same parameters used to calculate the base flow are used for the perturbation solution. For the MFP algorithm, the change in the base flow solution due to the Navier-Stokes operator is precomputed and

saved so that it can be subtracted from the total solution, \mathbf{Q}_t , after each timestep. This ensures that the base flow does not change and therefore, the resulting solution is only from the perturbation evolution. During each timestep, the instantaneous perturbation solution, $\mathbf{Q}' = \mathbf{Q}_t - \mathbf{Q}_b$, is recorded.

Snapshots of the instantaneous perturbation solution are used for DMD post-processing to find the dynamically most relevant structures. DMD computes a series of spatial modes that are each associated with a decay/growth rate ω_r and an oscillating frequency $\omega_i/(2\pi)$. These spatial modes can be represented as a series of N snapshots written as:

$$Q(\mathbf{x}, t) = \sum_{n=1}^N a_n \hat{Q}_n(\mathbf{x}) e^{\omega_n t} \quad (2)$$

where a and $\hat{Q}_n(\mathbf{x})$ represent the amplitude and spatial mode respectively, and $\omega_n (= \omega_r + i\omega_i)$ represents the frequency of the corresponding mode. For a linear system, ω_r and ω_i represent the temporal growth rate and frequency, and the DMD modes are the desired global linear stability modes. As will be done in the current study, by analyzing the largest growth rates ($w_r > 0 = \text{unstable}$) of the most relevant structures, DMD can be used to determine which temporal frequencies are the least stable and what is the corresponding spatial wavelength of that least stable mode. Detailed explanations of the MFP algorithm and DMD post-processing steps are shown in [4].

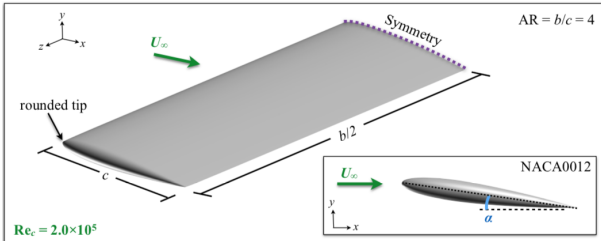
DETAILS OF THE COMPUTATIONS

Geometry and Flow Conditions

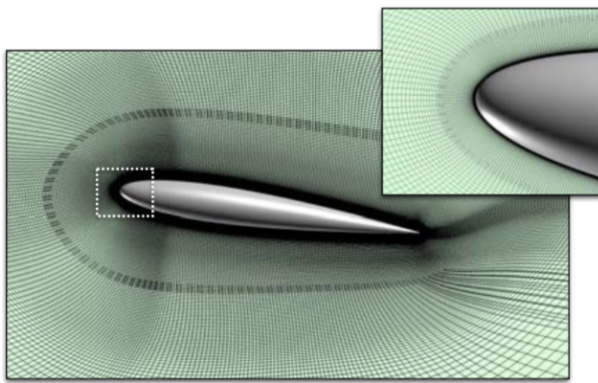
The geometry under consideration, depicted in Fig. 1(a), is a rounded tip, NACA0012 wing of aspect ratio $AR = b/c = 4$. The wing operates at a chord-based Reynolds number of $Re_c = 2 \times 10^5$ and free-stream Mach number $M_\infty = 0.1$ to largely avoid effects of compressibility for this stage of the analysis. An angle of attack corresponding to $\alpha = 12^\circ$ is examined. Additionally, the flow is assumed to be symmetric about the mid-span, so only half the wing is modeled.

Computational mesh and boundary conditions

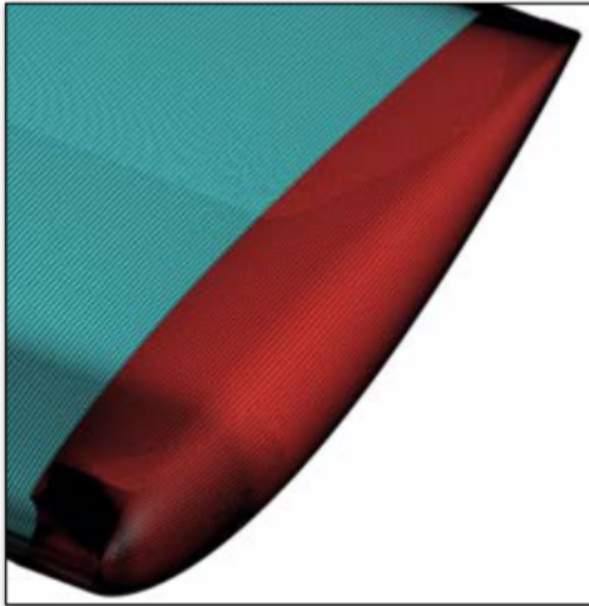
The domain around the wing is discretized using a series of nested meshes that utilize Chimera overset [7] to facilitate communication via high-order interpolation. [8]. An O-grid topology is employed around the airfoil profile, which is seen in Fig. 1(b) with every other gridline shown. The wing surface is prescribed with 1280 elements circumferentially and 1015 cells distributed along the half-span with a spacing of $\Delta z = 0.002c$ across the majority of the wing that decreases to a refined spacing of $0.0015c$ near the wingtip. The surface mesh is hyperbol-



(a) Wing configuration



(b) Airfoil section O-grid



(c) Tip cap C-grid

FIGURE 1: Wing configuration and mesh structure. Only every other gridline is shown in (b) and (c) for clarity.

ically marched in the normal direction with an initial off-body spacing of $\Delta n_i = 5.0 \times 10^5$ and increased stretching over 395

cells until reaching a distance of $100c$ from the airfoil surface. The fine circumferential and spanwise spacings are needed at the wall; however, they quickly become unnecessary away from the wing. Therefore, at normal distances of $0.03c$ (100 cells), $0.25c$ (200 cells), and $1.0c$ (300 cells), the O-grid is split into separate overlapping meshes to gradually coarsen the circumferential and spanwise directions by factors of $2/3$ of the original distribution at the first interface, $1/2$ at the second, and $1/4$ at the third.

A C-grid topology is used to discretize the rounded wingtip which is wrapped by 196 elements circumferentially and 762 cells along the chord as depicted in Fig. 1(c). This surface mesh is marched hyperbolically away from the body with a similar distribution as the O-grid, until reaching a normal distance of $1.0c$ (300 cells), where it oversets into a background mesh that extends another $50c$ outboard of the wingtip. An additional high resolution mesh, which is not shown here, is overset downstream of the leading edge that is aligned with the tip to maintain resolution of the generated tip vortex for up to three chords from the trailing edge. Even with overset grids with reduced levels of resolution away from the wing, the entire mesh system totals over 316 million cells.

For the base flow solution, the wing surface is set as a no-slip, adiabatic wall enforced by a third-order-accurate, zero-normal pressure gradient, and symmetry is employed at the midspan. The far-field boundary in the background mesh outboard of the wingtip is specified as an extrapolated outflow, while all other far-field boundaries are prescribed with uniform flow conditions. In the vicinity of the these boundaries (within 40 chords), an absorbing sponge zone [9] is prescribed by an addition of a source term in the governing equations of the form:

$$\mathbf{S} = \sigma J^{-1}(\mathbf{Q} - \mathbf{Q}_\infty) \quad (3)$$

where σ is a hyperbolic ramping function that is zero for the first 60 chords from the wing, transitions from zero to unity between 60 and 70 chords, and remains at unity for the remaining extent of the domain. The source term (Eq. (3)) acts to turn the flow towards its free-stream values and prevents spurious reflections from corrupting the domain interior.

For the MFP simulation, boundary conditions are only applied to the perturbation solution \mathbf{Q}' . The wing surface, midspan plane and farfield boundaries were set as a no-slip, adiabatic wall enforced by a third-order-accurate, zero-normal pressure gradient.

Assessment of spatial resolution

A measure of this grid system's spatial resolution has been provided previously by Garmann and Visbal [10] for an aspect-ratio-six wing at fixed incidence $\alpha = 8^\circ$ and Reynolds number

$Re = 2.0 \times 10^5$. In that study, convergence of the time-mean and instantaneous flow structure was demonstrated. The grid was also shown to maintain wall-normalized mesh spacings well within the recommendations of Georgiadis et al [11] for wall-resolved LES, who suggest $\Delta s^+ \leq 150$, $\Delta n^+ \leq 1$, and $\Delta z^+ \leq 40$ for streamwise, normal, and spanwise spacings, respectively. These values probed in the turbulent regions at $x/c = 0.8$ along the wing's mid-span, which actually represents the coarsest spanwise spacing on the surface, are $\Delta s^+ = 19.9$, $\Delta n^+ = 0.378$ and $\Delta z^+ = 15.6$. It should be noted that, while the wing used in this study utilizes a slightly smaller aspect ratio than the previous work, $AR = 4$ instead of 6, the mesh from the longer wing was simply truncated and the spacings were left unchanged.

NUMERICAL RESULTS

Base Flow Simulations

The baseflow instantaneous three-dimensional flow structure is shown in Fig. 2. Here, iso-surfaces of stagnation density, $(\rho_o/\rho_{o,\infty}) = 0.996$, are used to highlight the overall character of the vortex while masking the small-scale turbulent or transitional elements of the flow that may otherwise obscure the dominant features. The baseflow time-mean flow structure is provided in Fig. 3, where iso-surfaces of stagnation density are again utilized. Comparing the instantaneous and time-mean flow structures in Figs. 2 and 3, the unsteady shear-layer structures are evident in both the instantaneous and time-mean realization. This shows that these shear-layer structures over the wing are stationary events, i.e. fixed in time and space. Further details about the base flow can be found in Ref. [5].

MFP Simulations and DMD Analysis, $\alpha = 12^\circ$

The time-averaged mean flows from Fig. 3 were used for the MFP analysis. The initial random pressure perturbation that was added to the base flow near the leading edge of the wingtip is shown in Fig. 4. Time-mean velocity streamlines were seeded from the perturbation region to ensure that the perturbation would convect towards the trailing edge of the wingtip, where we are most interested in applying flow control. As mentioned previously, the perturbation amplitude is five orders of magnitude smaller than the free-stream values to ensure that evolution of the perturbation is linear.

The evolution of the pressure perturbations at the wingtip surface is shown with the contour plots in Fig. 5. After the initial perturbation is given, the perturbations start to coalesce on the wingtip surface after around $\tau = 2.0$ (see Fig. 5 (a)). As time progresses, a distinct structure forms near the wingtip trailing edge, as denoted by the black circle in Fig. 5 (c) and (d). This structure appears to have a spatial wavelength associated with it, although the specific wavelength is not clear from only observing the instantaneous perturbation solution. Figure 6 shows the

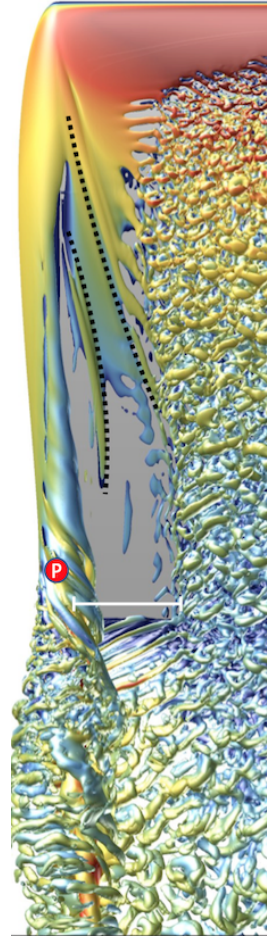


FIGURE 2: Instantaneous three-dimensional flow structure of the tip vortex shown through iso-surfaces of Q-criterion

instantaneous pressure perturbation at a probe located within this region at $x/c = 0.939$ (see red circles in Figs. 2, 3 and 5). For $\tau > 4.5$, there appears to be a dominant temporal frequency that is present. However, once again the specific temporal frequency is not clear from the pressure probe alone. Therefore, to extract these features from the solution, the DMD is applied over 250 pressure perturbation snapshots from $\tau = 5.4$ to $\tau = 6.4$. Using a higher sampling rate did not effect the result and thus, this sampling rate was deemed sufficient for the calculation. Since flow control will ultimately be applied along the surface, pressure data from the wingtip was used for the DMD analysis.

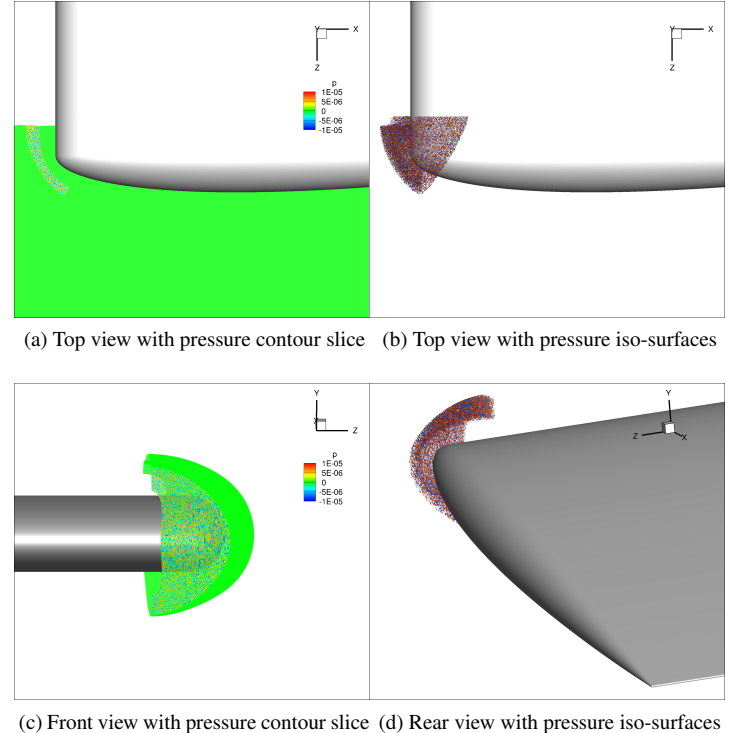
The dynamic modes obtained from the DMD are ranked according to their normalized amplitude [4], which is shown in the top portion of Fig. 7. In the normalization procedure, all DMD modes were normalized by the DMD mode with the maximum amplitude. DMD modes with a non-physical frequency ($\omega_i/2\pi < 1$) or were extremely stable (growth rate $\omega_r < -10$)



FIGURE 3: Time-mean vortex structure

were neglected when considering the maximum. Thus, there are few normalized amplitudes that are greater than unity. The modes with the highest amplitude (≈ 1) represent leading modes that are most relevant to the flow dynamics [12, 13]. The corresponding $\omega_i/(2\pi)$, and ω_r for the i^{th} leading mode are shown in the middle and bottom portions of Fig. 7, respectively. After ordering based on physical relevance, the modes were analyzed for the growth or decay of their amplitudes. Figure 8 shows the eigenspectrum of only the most dominant modes (defined as the normalized amplitude < 0.1), with the least stable mode of $\omega_r = 1.179$ and $\omega/2\pi = 5.526$ noted. The corresponding least stable mode shape is shown in Fig. 9, where a well defined spatial wavelength is seen near the wingtip trailing edge. This shows that the flow over the wingtip is receptive to flow control at this spatial wavelength at an excitation frequency of $\omega/2\pi = 5.526$.

The frequency of the least stable mode and its corresponding mode shape that was shown in Figs. 8 and 9 was found to be



(c) Front view with pressure contour slice (d) Rear view with pressure iso-surfaces

FIGURE 4: Initial random pressure perturbation that was added to the base flow near the leading edge of the wingtip. Top views are shown in (a) and (b), front view is shown in (c) and rear view is shown in (d).

dependent on how much of the initial transient data was removed prior to the DMD calculation. To arrive at a single solution rather than an infinite amount of solutions, the length of initial transient data skipped, τ_{skip} , was varied from 0.0 to 5.4 convective times, while keeping the total amount of sampling data constant at 250 snapshots over $\tau_{samp} = 1.0$. The result of this parametric sweep is shown in Fig. 10. For $\tau_{skip} \geq 4.5$ (see red vertical dashed line) a dominant least stable mode is consistently identified. This is shown more clearly in Fig. 11, where the cumulative average least stable mode frequency is calculated for the region $\tau_{skip} \geq 4.5$. There is some scatter in the data, but as shown by the relatively constant value of the cumulative average, there is a dominant least stable mode frequency at $\omega_{i,LSM}/(2\pi) \approx 5.52$. The consistent identification of such features across the range of analysis parameters gives more confidence in the DMD results, and shows the flow to be most susceptible to a definitive temporal frequency and spatial wavelength associated with the least stable mode.

In this analysis, the zero frequency mode, which is the most dominant mode, was not considered. The zero frequency mode

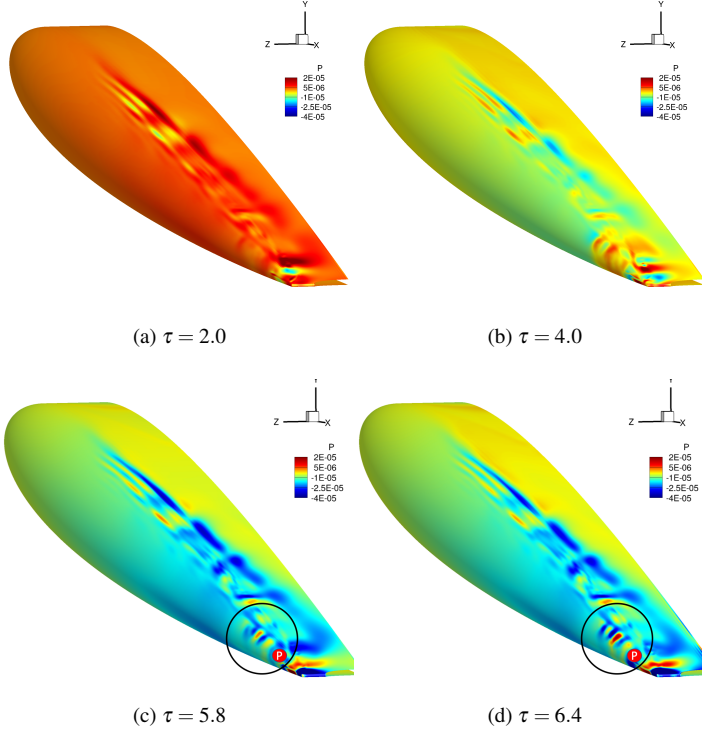


FIGURE 5: Instantaneous pressure perturbation field at (a) $\tau = 2.0$, (b) $\tau = 4.0$, (c) $\tau = 5.8$, and (d) $\tau = 6.4$.

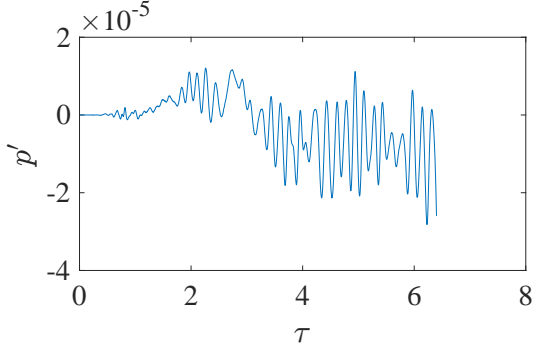


FIGURE 6: Instantaneous pressure perturbation at $x/c = 0.939$. Location of pressure probe with respect to the wing is shown with red circles in Figs. 2, 3 and 5.

is shown in Fig. 12. Interestingly, in the region inside the black circle, there is a clear spatial wavelength. Since this region occurs near the incipient separation of the tip vortex, perturbing this region with actuation at the same spatial wave length as the ob-

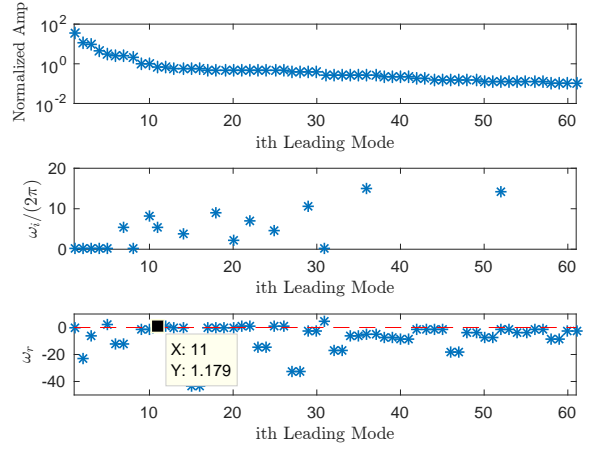


FIGURE 7: Normalized amplitude, frequency $\omega_i/(2\pi)$, and growth rate ω_r for the i^{th} leading mode. The least stable mode is shown.

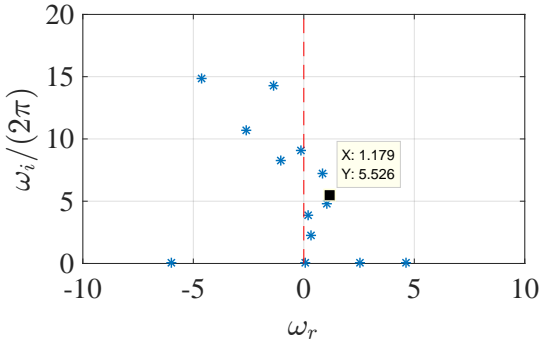


FIGURE 8: Eigenspectrum of the dominant modes. The least stable mode is shown.

served mode shape highlights another opportunity for exciting a strong response from the flow.

Finally, the time-mean x-vorticity and C_p near the airfoil surface is shown in Fig. 13 from the base flow (free of perturbation). Comparing Fig. 13 with the MFP results in Figs. 5, 9 and 12, it is clear that the MFP technique is able to extract receptivity modes that are otherwise not apparent in the mean-flow field alone. The spatial mode shape and frequency information resulting from the MFP also provide a unique starting to design flow control

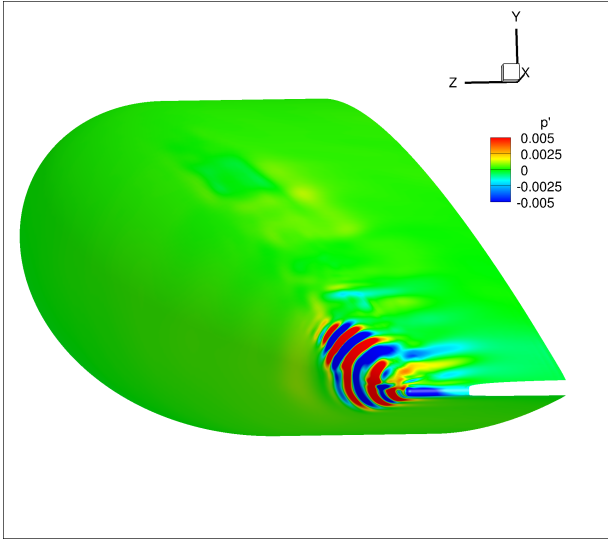


FIGURE 9: Eigenvectors of the least stable mode in perturbation pressure.

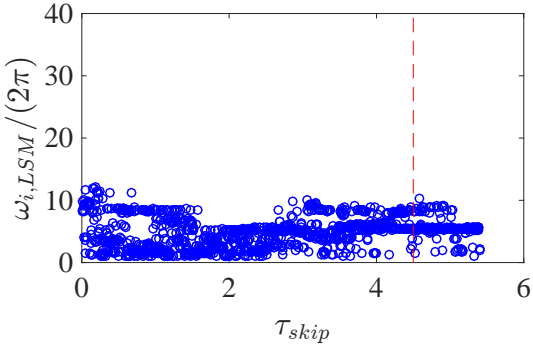


FIGURE 10: Distribution of frequency of the least stable modes $\omega_{i,LSM}/(2\pi)$ as different amounts of initial transients τ_{skip} are skipped from the DMD calculation. Vertical red dashed line denotes where the cumulative average begins.

CONCLUSIONS AND FUTURE WORK

The mean flow perturbation (MFP) technique was applied to a wingtip vortex problem previously studied by the authors. The aspect-ratio-four NACA0012, rounded-tip wing operated at $Re = 2.0 \times 10^5$ and incidence of $\alpha = 12^\circ$. The objective was to provide additional insight into the least stable mode (shapes and frequencies) associated with the vortex structure that could then inform targeted active flow control techniques. The evolved perturbations coalesced near the trailing edge along the tip, and uncovered the least-stable and dominant mode with a discrete spa-

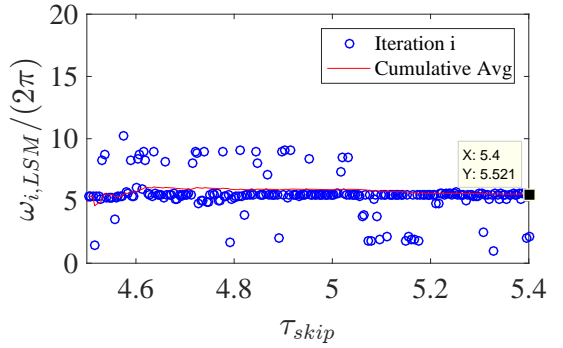


FIGURE 11: Distribution of frequency of the least stable modes $\omega_{i,LSM}/(2\pi)$ over the region that the cumulative average of the least stable mode is calculated.

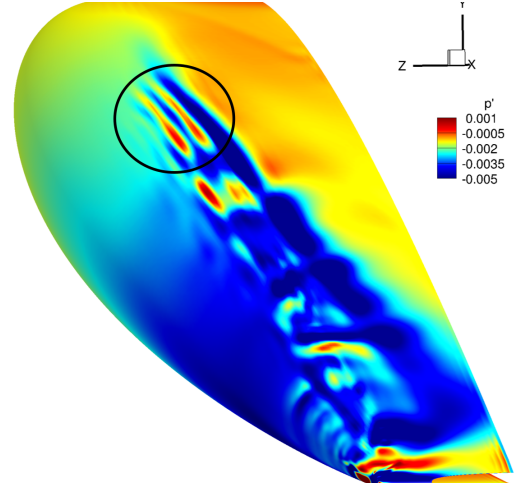


FIGURE 12: Eigenvectors of the zero frequency mode in perturbation pressure.

tial shape and temporal frequency. This mode provides a unique actuator design and operating condition tailored to the receptivity of the vortex itself, and therefore, could elicit a strong response. Another potential region for targeted actuation came from analyzing the zero-frequency mode, which revealed a clear spatial wavelength and discrete frequency near the incipient separation of the vortex. In either case, the MFP technique has extracted unique receptivity information and flow features that are not otherwise accessible from the mean- or instantaneous flows alone.

Future work will implement and assess the flow control designs garnered from the MFP analysis here, where the spatial

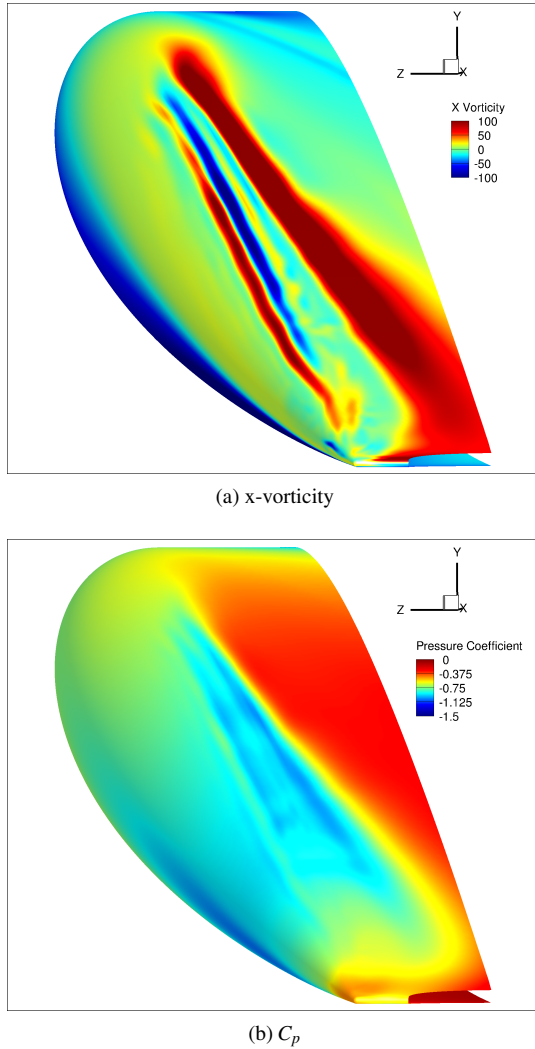


FIGURE 13: Time-mean (a) x-vorticity and (b) C_p near the airfoil surface.

modulation and temporal frequencies of the least-stable modes will be used drivers of the actuation.

ACKNOWLEDGMENT

This material is based, in part, under work supported by the Air Force Office of Scientific Research (AFOSR) under award number FA9550-17RQCOR393 monitored by Dr. G. Abate. Many helpful conversations with Drs. S. Benton of the Air Force Research Laboratory are gratefully acknowledged along with a grant of computing time from the Department of Defense High Performance Computing Modernization Program (DOD HPCMP).

REFERENCES

- [1] Gursul, I., and Wang, Z., 2018. “Flow control of tip/edge vortices”. *AIAA Journal*, **56**, 02, pp. 1–19. doi:[10.2514/1.J056586](https://doi.org/10.2514/1.J056586).
- [2] Margaris, P., and Gursul, I., 2010. “Vortex topology of wing tip blowing”. *Aerospace Science and Technology*, **14**, 04, pp. 143–160. doi:[10.1016/j.ast.2009.11.008](https://doi.org/10.1016/j.ast.2009.11.008).
- [3] Lee, S. C., Tavella, D., Wood, N. J., and Roberts, L., 1989. “Flow structure and scaling laws in lateral wing-tip blowing”. *Aiaa Journal - AIAA J*, **27**, 08, pp. 1002–1007. doi:[10.2514/3.10211](https://doi.org/10.2514/3.10211).
- [4] Ranjan, R., Unnikrishnan, S., and Gaitonde, D. V., 2018. “On the use of mean flow perturbation for global stability analysis”. In Fluid Dynamics Conference, American Institute of Aeronautics and Astronautics. doi:[10.2514/6.2018-3378](https://doi.org/10.2514/6.2018-3378).
- [5] Garmann, D. J., and Visbal, M. R., 2017. “Investigation of the unsteady tip vortex structure on a naca0012 wing at fixed incidence”. 2016 AIAA SciTech Meeting, American Institute of Aeronautics and Astronautics. doi:[10.2514/6.2017-1002](https://doi.org/10.2514/6.2017-1002).
- [6] Visbal, M. R., and Gaitonde, D. V., 2002. “On the use of higher-order finite-difference schemes on curvilinear and deforming meshes”. *Journal of Computational Physics*, **181**(1), pp. 155–185.
- [7] Steger, J. L., Dougherty, F. C., and Benek, J. A., 1983. “A chimera grid scheme”. *American Society of Mechanical Engineers, Fluids Engineering Division (Publication) FED*, **5**, 02.
- [8] Sherer, S. E., and Scott, J. N., 2005. “High-order compact finite-difference methods on general overset grids”. *J. Comput. Phys.*, **210**(2), Dec., pp. 459–496. doi:[10.1016/j.jcp.2005.04.017](https://doi.org/10.1016/j.jcp.2005.04.017).
- [9] Freund, J. B., 1997. “Proposed inflow/outflow boundary condition for direct computation of aerodynamic sound”. *AIAA Journal*, **35**(4), pp. 740–742. doi:[10.2514/2.167](https://doi.org/10.2514/2.167).
- [10] Garmann, D. J., and Visbal, M. R., 2016. “Unsteady evolution of the tip vortex on a stationary and oscillating naca0012 wing”. 2016 AIAA SciTech Meeting, American Institute of Aeronautics and Astronautics. doi:[10.2514/6.2016-0328](https://doi.org/10.2514/6.2016-0328).
- [11] Georgiadis, N. J., Rizetta, D. P., and Fureby, C., 2010. “Large-eddy simulation: Current capabilities, recommended practices and future research.”. *AIAA Journal*, **48**(8), pp. 1772–1784.
- [12] Schmid, P., 2011. “Application of the dynamic mode decomposition to experimental data”. *Experiments in Fluids*, **50**, 04, pp. 1123–1130. doi:[10.1007/s00348-010-0911-3](https://doi.org/10.1007/s00348-010-0911-3).
- [13] Mohan, A., and Gaitonde, D. V., 2017. “Analysis of airfoil stall control using dynamic mode decomposition”. *Journal of Aircraft*, **02**, pp. 1–13. doi:[10.2514/1.C034044](https://doi.org/10.2514/1.C034044).